iranpaper Downloaded from https://iranpaper.ir
https://www.tarjomano.com ترجمه تخصصی این مقاله مورد تایید ایران پیپر

Journal of Power Sources 548 (2022) 232084

Contents lists available at ScienceDirect

Journal of Power Sources

journal homepage: www.elsevier.com/locate/jpowsour

Computational modelling of paper-based capillary-driven microfluidic flow cells

P. Sadeghi , E. Kjeang *

Fuel Cell Research Lab (FCReL), School of Mechatronic Systems Engineering, Simon Fraser University, Surrey, BC, V3T 0A3, Canada

HIGHLIGHTS

- A dynamic mathematical model is developed for paper-based microfluidic flow cells.
- A 2D model can represent a 3D cell subject to Nernst-Planck equation refinement.
- The model reveals the unique working mechanism of imbibition and back-diffusion.
- Crossover is identified as the key limiting factor for cell performance and runtime.
- An optimized cell design is proposed with 3x performance improvement.

GRAPHICAL ABSTRACT

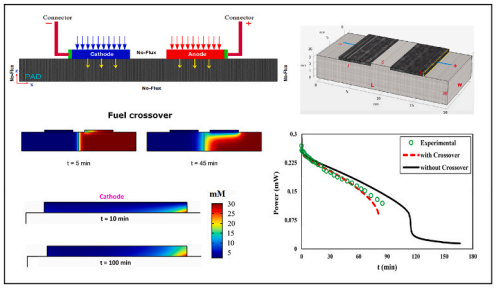

ARTICLE INFO

Keywords:
Flow cell
Capillary flow
PowerPAD
Imbibition
Richards equation
Quinone redox

ABSTRACT

A general mathematical model is developed for electrochemical energy conversion in paper-based, capillary-driven, microfluidic flow cells. A two-dimensional version of the model is implemented to simulate a novel flow cell of this kind called PowerPAD. The methodology developed is validated against experimental data for this particular cell under both steady and unsteady modes of operation. It is shown that a 2D model can represent a 3D cell in unsteady flows provided that the Nernst-Planck equation is properly refined. The results are interpreted in terms of transient back-diffusion and crossover of the reactant species which are found to be the key factors controlling the electrochemical performance of this cell. The validated model is used to enhance the power output, runtime, and energy efficiency of this particular cell through altering its flow architecture and microstructure of electrodes and absorbent pad. The refined cell design is shown to roughly triple the power output and runtime of the device. The optimized design also outperforms the original design in terms of energy efficiency. The developed mathematical model, the fundamental understanding, and the proposed cell design may be utilized to develop new devices and concepts for capillary-based electrochemical systems, including biodegradable batteries, fuel cells, and electrolyzers.

1. Introduction

Portable electronic devices such as laptops, cell phones, tablets, and smart-watches play a key role in our everyday life [1]. These small-sized devices need electricity to function and, at present, their power needs are generally met with metal-based dry cells such as lithium or cadmium

* Corresponding author.
E-mail address: ekjeang@sfu.ca (E. Kjeang).

https://doi.org/10.1016/j.jpowsour.2022.232084
Received 27 May 2022; Received in revised form 30 August 2022; Accepted 4 September 2022
Available online 15 September 2022
0378-7753/© 2022 Elsevier B.V. All rights reserved.

iranpaper Downloaded from https://iranpaper.ir
https://www.tarjomano.com ترجمه تخصصی این مقاله مورد تایید ایران پیپر

batteries. The problem with these conventional dry cells is that they are not renewable. Also, they can harm the environment through improper disposal [2]. For reasons like these, the search for new battery technologies is still ongoing. In a world re-imagined with sustainable energy, an ideal battery technology would be completely bio-degradable and eco-friendly. Certain types of fuel cells and flow batteries may meet these environmental criteria [3]. For instance, enzymatic biofuel cells produce electrical energy based on the capacity of naturally-occurring redox enzymes to reduce/oxidize a wide variety of fuels and oxidants [4]. Quinone-based flow batteries have also been developed for energy storage, using redox active reactants derived from natural products [5]. Although these technologies were primarily considered for large-scale storage systems, they can also be used in microfluidic flow cells [6,7] for powering portable devices such as rapid diagnostic kits [8]. Of particular importance are the paper-based diagnostic kits [9–11] which have the potential to be powered by microfluidic electrochemical cells. In recent years, paper-based microfluidic flow batteries and fuel cells have been developed for such low-power eco-friendly applications [12, 13]. Capillary flow plays a key role in the proper functioning of paper-based diagnostic kits. The concept of co-laminar flow can further enable electrochemical cells to function without an ion-exchange membrane. As such, they are increasingly being considered for powering e-kits used in diagnostic or environmental monitoring. It is anticipated that through further development, their range of applicability can be extended to cell phones or laptops. Further research in this area can also facilitate new forms of energy storage and offer inexpensive solutions for electrolytic power-to-gas and power-to-X conversion systems; see the recent review by Ibrahim et al. [14].

The functionality, energy conversion efficiency, service time, and power performance of paper-based microfluidic flow cells could be better understood and extended if a mathematical model were available to solve the coupled reaction-transport phenomena within the flow cells and predict their electrochemical performance. Such a model would enable investigation of the effects of different parameters on the system performance and thus reduce the requirements for exhaustive and costly trial-and-error driven experimental methods. At present, no such mathematical model is available in the open literature for designing paper-based microfluidic flow cells. In contrast, the literature is quite rich in theoretical models devised for designing *pressure-driven* microfluidic flow batteries and fuel cells operating under constant flow rate [15–18]. Nevertheless, there remains a considerable gap in the knowledge on the more recently developed paper-based microfluidic electrochemical cells [14]. A major problem in the development of mathematical models for paper-based flow cells is the *inhomogeneous* nature of these cells which is a consequence of the electrode material being different from the absorbent-pad material [19]. Further difficulty arises from the fact that a capillary-flow electrochemical cell is inherently a transient energy-conversion device wherein the system is initially unsaturated and remains partially saturated around the advancing front. Numerically resolving and/or tracking the liquid/air interface is a difficult task. Another challenge for membrane-less systems is to properly resolve the liquid/liquid interface and the related action of species crossover.

The objective of the present work is to develop a general mathematical model for predicting the electrochemical performance of paper-based microfluidic flow cells. As the first step, we formulate the separate equations governing electrolyte imbibition and electrochemical relationships, and show how they are coupled. This is followed by presenting the numerical scheme used to solve the coupled equations to simulate the operation and performance of the device. After validating the model with experimental data for a pioneering cell of this kind called PowerPAD [20]–a mixed-media water-activated biodegradable primary battery–the mathematical model is used to carry out a comprehensive parametric study in order to enhance the electrochemical performance of this cell. The work is concluded by summarizing its contributions to the field of microfluidic electrochemistry.

2. Mathematical model

The proposed mathematical modelling approach utilizes the following simplifying assumptions:

- Electrolytes are incompressible
- Physical and electrochemical properties of materials/species are constant
- Temperature is uniform throughout the domain
- Flow is occurring under laminar conditions
- Darcy's law is applicable
- Gravitational effects can be ignored
- Electrolytes are electrically neutral
- Formation of water in the cell is ignored
- Dilute-solution theory is applicable
- Migration term can be ignored
- Two-dimensional (2D) analysis is adequate

The 2D assumption is of crucial importance to our study as it requires that the Nernst-Planck equation should be properly revised; see Sec. 2.3. As the first step, we introduce the flow cell geometry used for this study.

2.1. Flow cell geometry

Fig. 1 shows the two-dimensional flow cell geometry used in this work. This figure also shows the Cartesian coordinate system used for mathematical development. The flow occurs in the xz-plane with the y-axis serving as the neutral direction. The electrolytes enter the electrodes from their top planes and flow directly through the porous electrodes until they enter the absorbent pad situated below the electrodes. As soon as the electrolytes enter the pad, they flow laterally until contact is made between anolyte and catholyte at the mid-plane of the pad (*i.e.,* where ions are exchanged between the two half cells of the device thus activating the electrochemical cell). The 2D cell geometry depicted in Fig. 1 resembles the flow architecture of the PowerPAD – a prospective, novel, paper-based, biodegradable, flow battery described in full details in Ref. [20]. The main difference between the present 2D model and the PowerPAD (which is a 3D device) is in the width of their respective absorbent pads which is 5 mm for our 2D model while it is 20 mm for the real cell; see Fig. 1b. The other geometrical parameters are the same between the two cells, with length of 20 mm and pad thickness of 0.83 mm. Also, both cells have the same electrode dimensions: 5 mm × 5 mm x 0.37 mm.

With the electrode and pad being initially dry, the mathematical model describing the transient device operation will necessarily comprise two parts: 1) imbibition modelling; and 2) electrochemical modelling.

2.2. Imbibition modelling

In the present work, we rely on the Richards equation for modelling the imbibition of electrolytes by the electrodes and the absorbent pad. Richards equation is a variation of the Darcy's law in which permeability and pressure terms are allowed to vary with moisture content. In vector form, the Richards equation reads as [21]:

$$\vec{q} = -\frac{k(S)}{\mu}[\vec{\nabla} p_c(S)], \tag{1}$$

where $\vec{q}$ is the flux, k(S) is the saturation-dependent permeability, and $p_c(S)$ is the saturation-dependent capillary pressure. In this equation, $S = \beta/\varepsilon$ is the degree of *saturation* for the wetting phase (where β is the volume of the liquid imbibed by the porous material), and ε is the total volume of its void spaces called *porosity*. Since β varies between 0 and ε, S varies between 0 and 1. The flux vector in the Darcy's equation can be related to the saturation field, S(**x**,t), through the continuity equation for

Downloaded from https://iranpaper.ir
https://www.tarjomano.com ترجمه تخصصی این مقاله مورد تایید ایران پیپر

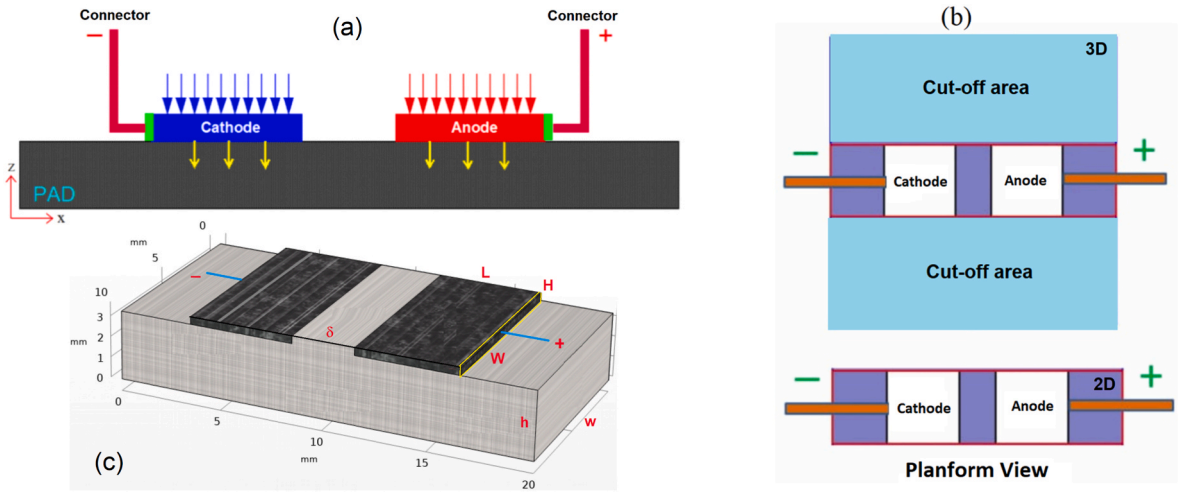

Fig. 1. (a) Schematic showing the frontal view of the 2D model used for the analysis; (b) planform view (in the z-direction) showing that the width of the 2D model is equal to the width of the electrode; and (c) the optimized 2D model used for the simulations. The electric current is collected from the terminals at the outer side-planes of the electrodes where the cell voltage is given as an input boundary condition.

the liquid phase; that is [21]:

$$\varepsilon\left(\frac{\partial S}{\partial t}\right) = -\nabla\cdot\vec{q}, \tag{2}$$

where t is the time and **x**(x,y,z) is the position vector. By combining Eq. (1) with Eq. (2) we can obtain the *mixed* form of the Richards equation, *i.e.*, the form that includes both saturation and capillary pressure:

$$\frac{\partial S}{\partial t} = \nabla\cdot\left(\frac{k(x,S)}{\varepsilon\,\mu}\nabla p_c\left(x,S\right)\right). \tag{3}$$

Although the mixed form is more appropriate for modelling multi-layered systems (as it enables pressure boundary condition to be imposed at the interface between the layers) the *saturation* form of the Richards equation is more appropriate for numerical simulations. To that end, we substitute:

$$\vec{\nabla}p_c\left(S\right) = \frac{\partial p_c}{\partial S}\vec{\nabla}S. \tag{4}$$

The Richards equation then becomes:

$$\frac{\partial S}{\partial t} = \nabla\cdot\left[\frac{k(S)}{\varepsilon\,\mu}\left(\frac{\partial p_c(S)}{\partial S}\right)\vec{\nabla}S\right] = \nabla\cdot[D(S)\vec{\nabla}S], \tag{5}$$

where $D(S)$ is the so-called *viscosity-scaled* diffusivity defined as:

$$D\left(x,S\right) = \frac{k(S)}{\varepsilon\,\mu}\left(\frac{\partial p_c(S)}{\partial S}\right). \tag{6}$$

Based on extensive experimental data obtained for granular materials, Brooks and Corey [22] proposed the following correlations for k(S) and p_c(S):

$$p_c(S) = p_{min}S^{-1/\lambda} \tag{7}$$

$$k(S) = k_{max}S^{3+2/\lambda} \tag{8}$$

where λ is a measure of the *tortuosity* of the porous material related to the pore-size distribution and connectivity between the pores. Assuming that the pores are spherical in shape and that their permeability can be represented by the Karman-Kozeny equation [23], p_{min} and k_{max} in the above relationships are written as [24]:

$$p_{min} = \frac{4\Gamma\cos\theta}{d_{max}}, \tag{9}$$

$$k_{max} = \frac{d_{max}^2}{180}\frac{\varepsilon^3}{(1-\varepsilon)^2}, \tag{10}$$

where Γ is the surface tension, θ is the contact angle, and d_{max} is the average pore size (called *retention* size in filter-paper terminology). Although the Brooks-Corey correlations were originally derived for granular materials such as soils, these correlations are also useful for fibrous materials [23]. The main difference between these two types of porous materials appears to be their k_{max} relationship. Specifically, for fibrous materials having a porosity larger than 80% it has been reported that the relationship $k_{max} = \varepsilon d_{max}/8$ is more accurate than Eq. (8) [24]. For the PowerPAD, however, the porosity of the electrode and pad is less than 80%, and Eq. (8) will be used. Based on the Brooks-Corey correlations, the viscosity-scaled diffusivity can be written as [25]:

$$D(S) = D_0\,S^m \tag{11}$$

where based on Eqs. (7)–(10) we have:

$$m = 2+\frac{1}{\lambda}\,;\quad D_0 = \frac{1}{\mu\,\varepsilon\,\lambda}\left(\frac{4\Gamma\cos\theta}{d_{max}}\right)\left(\frac{d_{max}^2}{180}\frac{\varepsilon^3}{(1-\varepsilon)^2}\right). \tag{12}$$

The two model parameters (m, D_0) can be theoretically obtained from Eq. (12) knowing the fluid and porous material parameters. For filter papers, Cruz et al. [25] directly obtained (m, D_0) by fitting Richards equation to the imbibition data extracted from the catalogues of the paper manufacturer. Either way, knowing (m, D_0) the Richards equation can be numerically solved to find the saturation field, S(**x**,t) from which we can find the flow rate. For the 2D model representing the PowerPAD (see Fig. 1a), liquid imbibition is restricted to the xz-plane, thus Richards equation becomes:

$$\frac{\partial S}{\partial t} = \frac{\partial}{\partial x}\left(D(S)\frac{\partial S}{\partial x}\right) + \frac{\partial}{\partial z}\left(D(S)\frac{\partial S}{\partial z}\right) \tag{13}$$

where S(x,z,t) is the *saturation* field. Having found S(x,z,t), we can compute the volume of liquid imbibed by a filter paper at any point in time as:

$$q(t) = \varepsilon\iiint_V S(x,z,t)dV = \varepsilon w\iint_A S(x,z,t)dA \tag{14}$$

where w is the width of the pad in the y-direction. Knowing q(t), we can calculate the instantaneous flow rate as shown below:

Downloaded from https://iranpaper.ir
https://www.tarjomano.com ترجمه تخصصی این مقاله مورد تایید ایران پیپر

$$Q(t) = \frac{dq}{dt} = \iiint_V \varepsilon \left(\frac{dS}{dt}\right) dv = \varepsilon w \iint_A \frac{dS}{dt} dx dz \tag{15}$$

The flow rate obtained this way can then be used to find the average velocity knowing the cross-sectional area of the material. We can then calculate the Reynolds number as a function of time in order to verify the validity of Darcy's law (which is the basis of the Richards equation). It is noteworthy that in the Richards equation, the effect of the non-wetting phase (*i.e.*, air) enters the problem only through the surface tension and contact angle; hence, the viscous resistance of the air is ignored. Whereas the Richards equation can accurately predict imbibition in many porous materials including filter papers [24,25], in its *classic* form this equation fails to predict the formation of finger-like structures sometimes observed in porous materials. As discussed in Ref. [26], the Richards equation is a linear diffusion-like parabolic equation; see, also [27]. With no inertial terms incorporated, interfacial disturbances cannot grow exponentially and lead to the formation of nonlinear finger-like structures at the liquid/air interface. Such instabilities are however unlikely to occur in the PowerPAD and related devices, wherein a more-viscous fluid displaces a less-viscous one. Gravitational effects due to density differences between the two fluids may also give rise to fingering instability, but again, the height of the device is likely too small for the gravitational force (counterbalanced by the viscous drag) to cause this instability. As discussed in the review by Rooij et al. [28], under certain conditions, large-scale systems such as those encountered in nature (*e.g.*, infiltration of rainwater into dry soils) may be vulnerable to fingering instability.

2.3. Electrochemical modelling

The paper-based microfluidic flow cell developed in Ref. [20], *i.e.*, the PowerPAD, is an all-quinone cell featuring the following electrochemical reactions:

$$H_2BQS \leftrightarrow BQS + 2H^+ + 2e^-; \qquad E_1^0 = -0.46 \ \text{V vs. SCE} \tag{16}$$

$$pBQ + 2H^+ + 2e^- \leftrightarrow H_2BQ \quad ; \qquad E_2^0 = +0.49 \ \text{V vs. SCE} \tag{17}$$

The kinetics is seen to involve two electrons which is one of the key features of the quinone redox couples used in Ref. [20]. In galvanic mode H_2BQS (hydroquinone sulfonic acid) serves as the fuel in the negative half-cell, whereas pBQ (para-benzoquinone) is the oxidant in the positive half-cell. In subsequent sections, the five active species involved in this device will be referred to by abbreviations (C_I, C_{II}, C_{III}, C_{IV}, C_V) corresponding to (H^+, H_2BQS, BQS, H_2BQ, pBQ). Based on the aforementioned reactions, the theoretical open-circuit cell voltage (OCV) is equal to 0.95 V. The experimental OCV, however, is around 0.80 V and this discrepancy must be resolved appropriately. To recover the experimental OCV, the Nernst equation can be revised as:

$$OCV = E^+ - E^- = 0.95 + \frac{RT}{2F} \ln\left(\frac{[C_{II}].[C_V].\left[\frac{\gamma_{H^+} C_{H^+}}{C_{acid,0}}\right]^2}{[C_{IV}].[C_{III}]}\right) - \Lambda \tag{18}$$

where T is the absolute temperature, F is Faraday's constant, C is the concentration, and γ is the activity coefficient. The experimental OCV can be recovered by simply setting: $\Lambda = 0.19$ V. Several parameters may contribute to the Λ-term with the Galvani potential drop being the most important one [28,29]. This potential drop arises when a common ion (here, proton) exists in two different electrolytes. When these two electrolytes are brought into direct contact with each other a potential drop is witnessed at the interface. This is because the mobility of the protons in the positive half-cell is different from that in the negative half-cell provided the mixed-media configuration of the PowerPAD cell [20]. In practice, this exhibits itself by a diffusional potential drop which can readily exceed 0.5 V [30].

Having modified the Nernst equation, next we proceed with formulating the unsteady analysis. In an electrochemical cell, electric current is generated when *active* species reach the surface of the electrodes and react electrochemically. By Faraday's first law, the rate of an electrode reaction is related to its current density as [31]:

$$\frac{\partial N}{\partial t} = \frac{j}{nF} \tag{19}$$

where $\partial N/\partial t$ is the number of moles of active species (N) reacting at each electrode per unit time, j is the current density, and n is the number of electrons. The net current of the cell (I) can be related to the anodic and cathodic current of each half-cell as shown below:

$$I = (j_{1,c} - j_{1,a})A = (j_{2,c} - j_{2,a})A \tag{20}$$

where A is the active surface area of the porous electrodes with subscripts (a,c) referring to the anodic and cathodic currents, respectively. In Eq. (20), subscript 1 refers to the cathode with subscript 2 referring to the anode. The current density of each electrode is related to the species concentrations (C) and activation overpotential (η) through the Butler-Volmer equation (BV) [31]:

$$j_{1,M} = FK_1 c_{IV}^{\alpha_{1,c}} c_V^{\alpha_{1,a}} \left[\frac{C_{IV}^s}{C_{IV}} \exp\left(\frac{+\alpha_{1,a} nF}{RT}\eta_1\right) - \frac{C_V^s}{C_V} \exp\left(\frac{-\alpha_{1,c} nF}{RT}\eta_1\right)\right] \tag{21}$$

$$j_{2,M} = FK_2 c_{II}^{\alpha_{2,c}} c_{III}^{\alpha_{2,a}} \left[\frac{C_{II}^s}{C_{II}} \exp\left(\frac{+\alpha_{2,a} nF}{RT}\eta_2\right) - \frac{C_{III}^s}{C_{III}} \exp\left(\frac{-\alpha_{2,c} nF}{RT}\eta_2\right)\right] \tag{22}$$

where K_1 and K_2 are the standard reaction-rate constants, and α is the charge transfer coefficient. In these equations, superscript s refers to the surface values whereas subscript M refers to the *main* reactions (in contrast to the *parasitic* reactions which will be denoted by subscript P in Sec. 2.4). Note that, as shown by Shah et al. [17], surface concentration is related to the activation overpotential using mass-conservation law for each ion/species (not shown here). The activation *overpotential* (η) can be related to the electrode potential as shown below:

$$\eta_c = (\varphi_s - \varphi_f)_c - E_c; \eta_a = (\varphi_s - \varphi_f)_a - E_a \tag{23}$$

where φ_s is the electronic potential of the electrodes, φ_f is the ionic potential (*i.e.*, the potential induced in the electrolyte due to the movement of *charged* species), and (E_a, E_c) are the *equilibrium* potential of the electrolyte at the surface of the anode and cathode, respectively. The equilibrium potential (E) can be found using the Nernst equation, as shown below [31,32]:

$$E = E_0 + \frac{RT}{nF} \ln\left(\frac{C_o^s}{C_r^s} \cdot \frac{\gamma_o}{\gamma_r}\right) \tag{24}$$

where E_0 is the thermodynamically-determined Nernst potential, and γ is the *activity* coefficient for the oxidant (subscript o) and reactant (subscript r) – they are known to be nearly equal to unity in dilute solutions. Thus, the current generated by an electrochemical cell is related to: i) the electronic potential (φ_s) applied to the electrode; ii) ionic potential (φ_f) induced in the electrolyte, and iii) reaction kinetics and overpotential. In general, three mechanisms can contribute to the mass transport in a flow cell: i) convection, ii) diffusion, and iii) migration. The total molar flux (**N**) can then be written as [32].

$$\mathbf{N}_{tot} = \mathbf{N}_{conv} + \mathbf{N}_{diff} + \mathbf{N}_{mig} = \mathbf{u}_j C_i - D_i \vec{\nabla} C_i - Z_i \xi_i (C_i \vec{\nabla} \varphi_f) \tag{25}$$

where Z_i is the species charge number, ξ_i is the *mobility* of each species, and C_i is the concentration of the species in the bulk. Note that in this equation **u** is the velocity field with subscripts j = 1,2 referring to the positive and negative half-cells, respectively. For a fully-saturated porous electrode (S = 1), based on the Nernst-Planck (NP) equation, conservation of mass requires that we should have [32]:

Downloaded from https://iranpaper.ir
https://www.tarjomano.com ترجمه تخصصی این مقاله مورد تایید ایران پیپر

$$\varepsilon\left(\frac{\partial C_i}{\partial t}\right) + \vec{\nabla}.\mathbf{N}_i = 0. \quad (26)$$

For dilute solutions, mobility can be written in terms of diffusivity as [32]:

$$\xi_i = \frac{F}{RT}D_i \quad (27)$$

The NP equation can then be written as:

$$\varepsilon\left(\frac{\partial C_i}{\partial t}\right) - D_i\nabla^2 C_i + \mathbf{u}_j \cdot \vec{\nabla}C_i - z_i\frac{F}{RT}D_i\left(C_i\nabla^2\varphi_f + \vec{\nabla}C_i \cdot \vec{\nabla}\varphi_f\right) = 0 \quad (28)$$

For active species (H_2BQS and pBQ) that reside inside the electrodes, the NP equation needs a source term (Θ) on the right-hand-side of Eq. (28), which is proportional to the current density of the given electrode [17]:

$$\Theta_{II} = -\Theta_{III} = -\frac{aj_2}{F}, \quad (29)$$

$$\Theta_V = -\Theta_{IV} = -\frac{aj_1}{F}, \quad (30)$$

where a is the specific active area of the electrode. The source term, Θ, can be related to species concentration as shown below [17]:

$$\Theta_i = [k_m A(C^s - C)]_i \quad ; \quad i = 1, 2, \ldots, 5 \quad (31)$$

where k_m is the mass-transfer coefficient which is controlled by many parameters such as viscosity/density of the electrolyte, tortuosity/porosity of the electrode, diffusivity of the ions/species, and the diameter of the electrode's carbon fibers. The dimensionless mass-transfer coefficient, called Sherwood number (Sh), is correlated with the Reynolds number (Re) and the Schmidt number (Sc) as shown below [33,34]:

$$Sh = n_1 + n_2(Re^{n_3}Sc^{n_4}) \quad (32)$$

where n_1, n_2, n_3, and n_4 are fitting parameters. In this relationship, n_1 is the so-called *diffusion-limited* Sherwood number reported to be around 2 [33,34]. The following relationship has been used in this work for calculating the Sherwood number [35]:

$$Sh = 2 + 0.018\left(Re^{0.68}\ Sc^{0.50}\right) \quad (33)$$

The dimensionless numbers in Eq. (32) are defined as shown below:

$$Sh = \frac{k_m d_f}{D}; \quad Re = \frac{U d_f}{\mu}; \quad Sc = \frac{\mu}{\rho D} \quad (34)$$

where d_f is the fiber dimeter, U is the *superficial* velocity (*i.e.,* the flow rate divided by the projected area of the electrode), and ρ is the density. For porous electrodes, we should replace diffusivity (D) of the ions with an *effective* diffusivity (D_{eff}). Using the Bruggeman correlation we have [36]:

$$D_{eff} = \varepsilon^{1.5}D \quad (35)$$

Next, we relate the current density of each electrode (j) to its local current density vector (**i**). Since the total charge is conserved during the electrochemical reactions, we can write:

$$aj_1 = \left(\nabla.\mathbf{i}_f\right)_1 = -\left(\nabla\cdot\mathbf{i}_s\right)_1 \quad (36)$$

$$aj_2 = \left(\nabla.\mathbf{i}_f\right)_2 = -\left(\nabla\cdot\mathbf{i}_s\right)_2, \quad (37)$$

where $\mathbf{i}_f$ and $\mathbf{i}_s$ represent ionic and electronic current density vectors, respectively. The electronic current density vector can be related to the electronic potential of the electrode using Ohm's law; that is:

$$\mathbf{i}_s = -\sigma_s\vec{\nabla}\varphi_s, \quad (38)$$

where σ_s is the nominal electronic conductivity of the electrode material. Since for porous electrodes the conductivity is less than its nominal value, we need the *effective* electronic conductivity for such electrodes. Using the Bruggeman correlation we have [36]:

$$\sigma_{s,eff} = (1-\varepsilon)^{1.5}\sigma_s \quad (39)$$

By taking the divergence of Eq. (38), we can relate an electrode's potential to its current density. The result is the Poisson equation which is a linear PDE from which we can obtain the electrode potential knowing its current density:

$$\sigma_s\left(\nabla^2\varphi_s\right) = aj_1 \quad (40)$$

To find the ionic potential, we start by noting that the ionic current density vector can be written as [32]:

$$\mathbf{i}_f = F\sum_{i=1}^{5} Z_i\mathbf{N}_i \quad (41)$$

where **N** can be obtained from Eq. (25). Thus, in practice, the ionic current-density vector is governed by the bulk concentration, ionic potential, and velocity field of the electrolyte. Since under creeping-flow conditions the velocity components are vanishingly small and also because the dilute electrolytes involved in the PowerPAD are electrically neutral (*i.e.*, $\sum_k z_k C_k = 0$), as shown in Ref. [32] the convective term can be dropped from the NP equation so that we have:

$$\mathbf{i}_f = -F\sum_{i=1}^{5} Z_i D_i\vec{\nabla}C_i - \sigma_f\vec{\nabla}\varphi_f \quad (42)$$

where σ_f is the electrolyte conductivity defined as:

$$\sigma_f = \frac{F^2}{RT}\sum_i Z_i^2 D_i C_i \quad (43)$$

To find the ionic potential, φ_f, we take the divergence of Eq. (42) to obtain:

$$-\sigma_f\nabla^2\varphi_f + F\sum_i D_i z_i\left(\nabla^2 C_i\right) = aj_1 \quad (44)$$

where we have assumed that the current is collected from the cathode. In cases where we can ignore the migration flux, the concentration term is eliminated from this equation and we end up with another Poisson equation this time for the ionic potential:

$$-\sigma_f\nabla^2\varphi_f \approx aj_1 \quad (45)$$

The migration term can indeed be dropped from the NP equation for the PowerPAD. In fact, in Ref. [37] it has been numerically shown that its effect on the cell performance is less than 5%. With ohmic loads on the order of $10^3\ \Omega$, the cell always operates at very low current densities [20]. Moreover, since the mobility of protons is an order of magnitude larger than that of quinone species, the energy of the electrostatic force is absorbed by these ions so that it has limited effect on the mass transfer of the redox couples. The favorable model validation against experimental data for the PowerPAD (see Sec. 4) implicitly corroborates this conclusion. With no convection and migration terms, the Nernst-Planck equation (Eq. (28)) is reduced to the following form:

$$\varepsilon\left(\frac{\partial C_i}{\partial t}\right) - D_{i,eff}\nabla^2 C_i = 0 \quad (46)$$

where the *nominal* diffusivity has been replaced with the *effective* diffusivity.

2.4. Crossover analysis

Microfluidic flow cells that lack a membrane to separate the two half-

iranpaper Downloaded from https://iranpaper.ir
https://www.tarjomano.com ترجمه تخصصی این مقاله مورد تایید ایران پیپر

cells of the device are known to be vulnerable to species crossover, and PowerPAD is no exception [38]. To model the crossover-induced parasitic electrochemical side-reactions for the PowerPAD, we consider two electrochemical reactions on each electrode with one being the *main* reaction and the other the *parasitic* reaction. For instance, on the cathode the main electrochemical reaction is the reduction of pBQ and the parasitic electrochemical reaction is the oxidation of H_2BQS which has crossed over from the negative half-cell. Similarly, on the anode the *main* reaction is the oxidation of H_2BQS and the *parasitic* reaction is the reduction of pBQ which has crossed over from the positive half-cell. On both electrodes the parasitic reactions are concerned only with the active species and they lower the net current generated by that specific electrode. As in Ref. [39], we assume that the parasitic side-reactions occur at the overpotential of the electrode subjected to crossover. Hence, for the parasitic electrochemical reactions (denoted by subscript "P") we can write:

$$j_{1,P} = FK_2 \; c_{IV}^{\alpha_{1,c}} \, c_V^{\alpha_{1,a}} \left[\frac{C_{II}^s}{C_{II}} \exp\left(\frac{+\alpha_{1,a} nF}{RT} \eta_2 \right) - \frac{C_{III}^s}{C_{III}} \exp\left(\frac{-\alpha_{1,c} nF}{RT} \eta_2 \right) \right], \tag{47}$$

$$j_{2,P} = FK_1 \; c_{II}^{\alpha_{2,c}} \, c_{III}^{\alpha_{2,a}} \left[\frac{C_{IV}^s}{C_{IV}} \exp\left(\frac{+\alpha_{2,a} nF}{RT} \eta_1 \right) - \frac{C_V^s}{C_V} \exp\left(\frac{-\alpha_{2,c} nF}{RT} \eta_1 \right) \right], \tag{48}$$

where we have assumed that when an active species crosses to the opposite half-cell, its kinetic parameters remain intact. Knowing the parasitic current density, we can find the net current density (j), at any given cell voltage, as shown below [40]:

$$j_{net} = (j_{2,M} - j_{2,P}) - (j_{1,M} - j_{1,P}) = (j_{2,M} - j_{1,M}) - (j_{2,P} - j_{1,P}) \tag{49}$$

The concentration of the active quinone species involved in the parasitic reactions should then satisfy the following equations:

$$\frac{dC_{II}}{dt} = D_{II} \nabla^2 (C_{II}) - \frac{j_{2,M}}{F} - \frac{j_{2,P}}{F} \tag{50}$$

$$\frac{dC_V}{dt} = D_V \nabla^2 (C_V) - \frac{j_{1,M}}{F} - \frac{j_{1,P}}{F} \tag{51}$$

$$\frac{dC_{III}}{dt} = D_{III} \nabla^2 (C_{III}) + \frac{j_{2,M}}{F} \tag{52}$$

$$\frac{dc_{IV}}{dt} = D_{IV} \nabla^2 (C_{IV}) + \frac{j_{1,M}}{F}. \tag{53}$$

3. Numerical method

We have employed the finite-element software package COMSOL Multiphysics (5.5) for solving the Richards equation for the liquid imbibition and the electrochemical equations for the cell power output. These equations were defined using appropriate scripts in the PDE module of this software. We have used the kinetic data given in Ref. [41] at state-of-charge SOC = 95%. Table 1 presents the kinetic parameters used in our simulations. We also need the diffusion coefficient of *proton* (H+) that is equal to 9.30 x 10^{-5} cm^2/s.

The concentration of H_2BQS (fuel) used in the PowerPAD was 0.2 M dissolved in 2 M potassium hydroxide (KOH) as the anolyte, whereas the concentration of pBQ (oxidant) was 0.2 M dissolved in 1 M oxalic acid ($C_2H_2O_4$). Table 2 presents the reference concentration for the four quinone species involved in the cell together with the concentration of the electrolytes used in the PowerPAD.

The simulations also require that the Richards equation parameters (m,D_0) are given as input for the electrodes and the absorbent pad materials. The technique described in Ref. [25] was used to obtain the absorbent pad parameters (m,D_0). For the electrodes, with no imbibition data available, they were calculated using Eq. 12. Table 3 presents the Richards' equation parameters for both materials.

In the next sub-section, the numerical scheme developed in this work is validated against experimental data reported in Ref. [20] for the PowerPAD.

3.1. Model validation: steady mode

In order to validate the mathematical/numerical model, the first step is to simulate the steady cell polarization curves for the PowerPAD and compare them with the experiments [20]. Polarization curves are normally obtained under steady state whereas the present model is transient. To that end, we need appropriate initial and boundary conditions for S,C, and φ_s. For S, we assume that the material is initially dry (S = 0). At the inlet section of the electrodes we fix the saturation at S = 1 at all times with no-flux used on all other planes. For the concentration, at inlet we have C = 0.19 M for the active quinone species and C = 0.01 M for the other quinone species (based on SOC = 95%). We set no-flux boundary condition for the concentration of quinone species on all other planes. As to the initial and boundary conditions on the electrode surfaces, the anode electric potential is set to ground whereas the cathode potential (*i.e.*, the cell-voltage, V_{cell}) is set at a prescribed value less than OCV = 0.8 V on its outer side plane, where the current is collected (see Fig. 1a). On all other surfaces we set zero-gradient (insulation) as the boundary condition. As soon as the level of saturation in the pad reaches equilibrium we record the current generated by the cell at that point in time (roughly 12 s after cell activation) and use the (V,I) pair as a single point on the steady polarization curve. By obtaining many such points, we construct the *quasi-steady* polarization curve by fitting a smooth curve between the points. Fig. 2a shows typical polarization curves computed in this way for three different absorbent pad thicknesses together with the experimental data reported in Ref. [20] for PowerPAD. The numerical results are in good agreement with the experimental data for all three cases. It is interesting to note that improved performance was achieved with thicker absorbent pads. This is due to reduced ohmic resistance for ion exchange at the contact line between the two electrolytes on the mid-plane of the pad.

Fig. 2b shows the corresponding power-performance curves as a function of the applied load. A strong dependency on the external load is observed, with peak power at relatively low load. For any given pad thickness, the load at peak power is much smaller than the load used in the experiments [20]. The simulated power curves thus demonstrate that PowerPAD can reach considerably higher power for external loads in the range of 100–200 Ω rather than 1000–2000 Ω, as used in the experiments [20]. It can be shown that at peak power, roughly three-quarters of the voltage drop (which is nearly 0.4 V) is caused by the ohmic resistance, which is hence the main limiting factor for the power-performance of the device. With the electronic resistance of the

Table 1
Kinetic parameters of the quinone species used in the PowerPAD [41].

Species	Diffusion Coefficient (D) ($cm^2.s^{-1}$)	Charge Transfer Coefficient (αn)	Rate Constant (K) ($cm.s^{-1}$)
H_2BQS/ BQS*	5.03 x 10^{-6}/5.03 x 10^{-6}	0.508	2.36 x 10^{-3}
pBQ/ H_2BQ*	3.80 x 10^{-6}/3.80 x 10^{-6}	0.582	1.55 x 10^{-4}

*With no data available for BQS and H_2BQ, we used published data for H_2BQS and pBQ for them.

Table 2
Reference concentrations of the species involved in the PowerPAD for SOC = 95%.

Species	Concentration (M)	Role
H_2BQS/BQS	0.19/0.01	Fuel/Product
pBQ/H_2BQ	0.19/0.01	Oxidant/Product
$C_2H_2O_4$	1.0	Catholyte
KOH	2.0	Anolyte

iranpaper Downloaded from https://iranpaper.ir
https://www.tarjomano.com ترجمه تخصصی این مقاله مورد تایید ایران پیپر

Table 3
Richards model parameters (m,D_0) used in this work.

Material	Application	m	D_0 (cm^2/s)	h (μm)	ε (%)	d_p (μm)
Toray TGP–120	Electrode	6.0	1.41 x 10^{-4}	370	78	28
Ahlstrom 222	Absorbent pad	2.6	1.11 x 10^{-5}	830	70	18

h = Thickness; ε = Porosity; d_p = Pore diameter; d_f = Fiber diameter.

electrodes being very small, one can conclude that the ohmic resistance of the cell is dominated by the ionic resistance; see Ref. [37] for more details.

3.2. Model validation: unsteady mode

In principle, paper-based microfluidic flow cells such as the PowerPAD can generate electricity as soon as the cell is activated by a drop of water. However, this initial device activation process is relatively brief. As shown by the modelling results in Sec. 4.1, full porous media saturation takes less than 15 s. For reference, the fully-saturated cell in Ref. [20] could generate power for roughly an hour. Hence, the unsteady results reported in Ref. [20] (after initial activation) can be used for further model verification and analysis. Note that the unsteady mode corresponding to battery discharge is a dynamic process given the finite content of reactants upon saturation of the device. Therefore, the SOC is time dependent based on the gradual conversion of reactants. For the PowerPAD the SOC can be defined for each half cell as shown below [42]:

$$SOC^- = \frac{[c_{II}]}{[c_{II}] + [c_{III}]}; \quad SOC^+ = \frac{[c_V]}{[c_V] + [c_{IV}]} \tag{54}$$

where, for a balanced cell, we have: $SOC = SOC^+ = SOC^-$. Given the SOC at t = t_0 we can obtain SOC at a later time $t = t_1 > t_0$ using the following equation [42,43]:

$$SOC(t_1) = SOC(t_0) - \frac{\int_{t_0}^{t_1} I(t)dt}{q_{th}} \tag{55}$$

where q_{th} is the theoretical capacity defined as [43]:

$$q_{th} = n \cdot C_0 \cdot q \cdot F \tag{56}$$

In this equation, C_0 is the initial concentration and q is the total volume of the electrolyte. Fig. 3 schematically shows what happens when an external load is connected to the PowerPAD. The point at which the load line and the polarization curve cross each other is called the *operating point*. For any given pad thickness and any given load, since the capacity of the cell is limited, the operating point shifts downward with the elapse of time. This implies that, for any given load, the cell generates gradually less current (and therefore less power) as time progresses.

Knowing the (V,I) of the operating points at different times, we can plot the power output as a function of time thereby determining the dynamic discharge behavior of the PowerPAD. To that end, we need the (V,I) coordinates of the operating points at t = 0 before we can march in time. Table 4 shows the operating point for the three pads for R_{ex} = 2000 Ω.

The numerical scheme developed in the present work requires that the cathode potential φ_s is given. Although, it is indeed given as an input at t = 0 (see Table 4), during the unsteady mode of operation it must be calculated before it is fed to the electrochemical solver. To that end, knowing the cathode potential at t = 0, we first find the current at t =

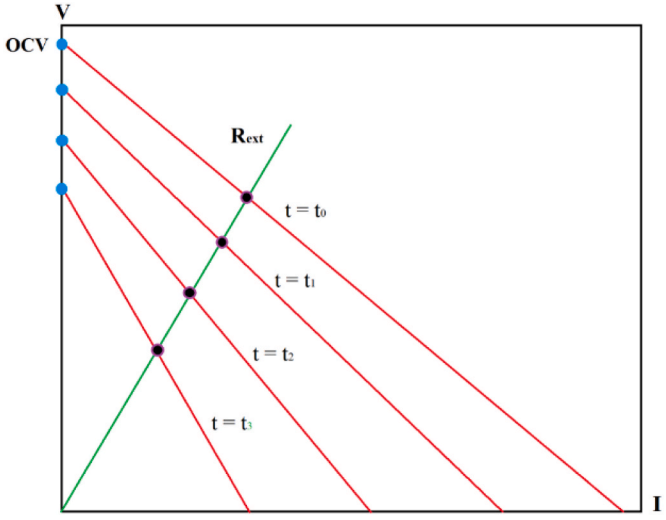

Fig. 3. Schematic showing the progressive decay of the operating point and the polarization curve of the PowerPAD for continuous operation under load.

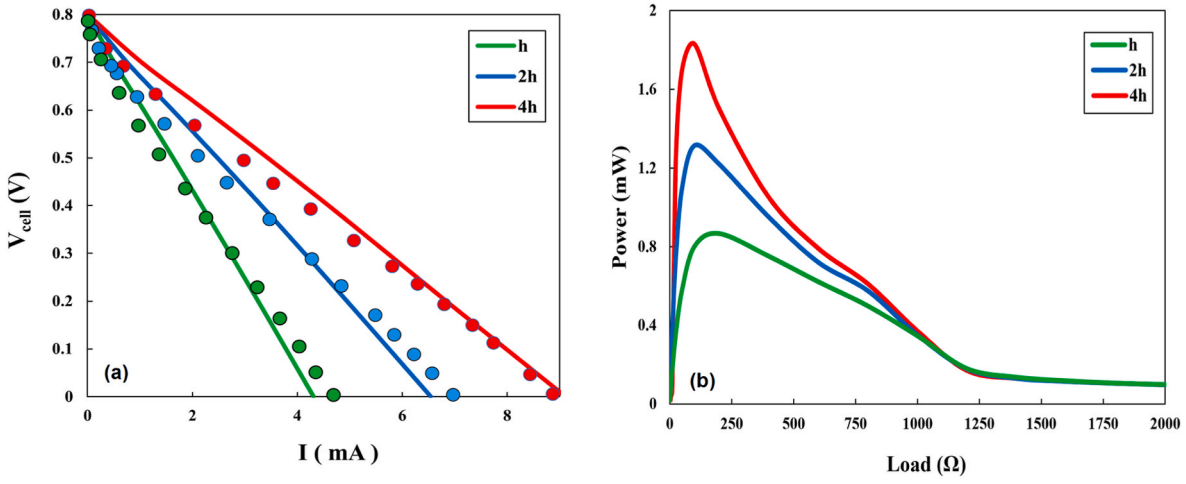

Fig. 2. (a) Polarization curves for PowerPAD capillary flow cells with different absorbent pad thickness (h). The simulated results shown by lines are compared to digitized experimental data from Ref. [20] shown as symbols; (b) power-performance curves as a function of external load
Note that on average 15,000 elements were used in these simulations to ensure grid-independency. A personal core i7 computer was used for the computations and each run took roughly 30 min to converge, owing to the 2D nature of the model.

iranpaper Downloaded from https://iranpaper.ir
https://www.tarjomano.com ترجمه تخصصی این مقاله مورد تایید ایران پیپر

Table 4
The operating points at t = 0 for R_{ext} = 2000 Ω.

PAD Thickness	Voltage (V)	Current (mA)	Power (mW)
h	0.728	0.365	0.266
2h	0.750	0.377	0.282
4h	0.763	0.380	0.290

0 using Ohm's law. Since this law should be valid at any time t > 0 thus we have:

$$I(t) = \frac{\varphi_s(t)}{R_{ext}} \tag{57}$$

On the other hand, conservation of charge requires that for the cathode we should have:

$$\nabla \cdot \vec{i}_s = -\sigma_s^{eff} \nabla^2 \varphi_s = -a j_1 \tag{58}$$

where $\vec{i}_s(x,z)$ is the current density vector in the electrode. By integrating this equation over the whole volume of the cathode, the current (I) is obtained as:

$$\iiint_{\forall} -\sigma_s^{eff} \nabla^2 \varphi_s d\forall = \iiint_{\forall} -a j_1 d\forall = I(t) \tag{59}$$

The volume integral on the left-hand-side can be converted to surface integral so that we have:

$$-\sigma_s^{eff} \; W \left[\iint_A \left(\frac{\partial^2 \varphi_s}{\partial x^2} dx \right) dz + \iint_A \left(\frac{\partial^2 \varphi_s}{\partial z^2} dz \right) dx \right] = I(t) \tag{60}$$

In the PowerPAD, electric current is collected through the outer side-plane of the cathode, *i.e.,* where we apply the potential boundary condition (see, Fig. 1a). Thus, we have:

$$W \int_0^{H_e} \sigma_s^{eff} \left(\frac{\partial \varphi_s}{\partial x}\bigg|_{x=16} - \frac{\partial \varphi_s}{\partial x}\bigg|_{x=4} \right) dz + W \int_0^{L_e} \sigma_s^{eff} \left(\frac{\partial \varphi_s}{\partial z}\bigg|_{z=H_e} - \frac{\partial \varphi_s}{\partial z}\bigg|_{z=0} \right) dx = I \tag{61}$$

where W, H_e, and L_e are respectively the width, height, and length of the electrode. Hence, the current collected by the current-collector should simultaneously satisfy the following equation:

$$I(t) = W \int_0^H -\sigma_s^{eff} \left(\frac{\partial \varphi_s(t)}{\partial x} \right) dz \tag{62}$$

By equating Eq. (57) with Eq. (62), the following integro-differential equation is obtained for the cathode potential which must be satisfied as boundary condition at all times t > 0:

$$\varphi_s + W R_{ext} \sigma_s^{eff}(t) \int_0^H \left(\frac{\partial \varphi_s}{\partial x} \right) dz = 0 \tag{63}$$

Eq. (63) is hence solved numerically at each time step. A solution to this equation yields $\varphi_s(t)$ which is actually the cell voltage (V_{cell}) since the internal cell resistance is negligible compared to the load. Knowing $\varphi_s(t)$, I(t) can be obtained from Eq. (57) to reveal the operating points in Fig. 3 as a function of time. From these results, the power output can be calculated and plotted as a function of time. The I(t) results can also be used to compute the cell efficiency as a function of the elapsed time [13]:

$$\eta_F = \frac{\int_0^t I(\tau) d\tau}{q_{th}} \tag{64}$$

$$\eta_E = \frac{\int_0^t I(\tau) V(\tau) d\tau}{E_0 q_{th}} \tag{65}$$

where η_F is the faradaic efficiency and η_E is the energy efficiency [13]. In these relationships, I(t) and V(t) are the time-dependent current and cell potential at the operating points with E_0 being its theoretical Nernst potential. During the unsteady mode of operation, however, the concentrations of active species drop with time. As a result, in order to represent a 3D cell such as PowerPAD by a 2D model, certain adjustments to the Nernst-Planck equation are necessary. While for the 3D cell, Eq. (46) is a good approximation for the NP equation, for the 2D model the temporal and diffusion terms in this equation need correction coefficients. This is because in the 2D model, diffusion of species occurs only in the xz-plane whereas in the 3D system it also occurs through the yz-plane and xy-plane. In the 3D system, diffusion of species from the absorbent pad to the electrode in the y-direction makes the concentration field more uniform in the yz-plane and weakens the concentration gradient in the xz-plane. In the present 2D model, this is accommodated by incorporating a 3D diffusion correction factor for the effective diffusivity term. For the 3D PowerPAD cell geometry, this correction factor is ¼. Additionally, the quantity of species stored inside the pad in 3D is roughly four times that of the 2D system, which is compensated for in the unsteady concentration term. With these two corrections included, for the 2D model, the revised NP equation becomes:

$$4\left(\varepsilon \frac{\partial C_i}{\partial t} \right) - \left(\frac{1}{4} D_i^{eff} \right) \nabla^2 C_i = -\Theta_i \tag{66}$$

where the subscript i refers to each ion. We assume that at t = 0 the concentration field is uniform with SOC = 0.95. All boundary conditions are the same as those used for the steady analysis with the only difference being no-flux boundary condition for the concentration of active species at the inlet plane of the electrodes. Also, for the pad we set the saturation at S = 0.93, which is its equilibrium saturation; see Sec. 4.1.

Fig. 4 shows a comparison between the numerical results obtained using the refined 2D model (lines) with the experimental data (symbols) reported for the real 3D PowerPAD cell [20]. The comparisons show that the model is able to correctly capture the dynamic power curves of the experimental device for two different absorbent pad thickness and two different external loads (with a maximum error of less than 10%) including the inherent decay in power output over time as the finite quantity of reactants is consumed. In the next section we show that the comparison can be further improved by including the crossover-related parasitic side-reactions in the analysis. Overall, these results demonstrate the effectiveness of the developed model for simulation of time-dependent operation of complex paper-based electrochemical cells.

4. Results and discussion

In this Section, we present 2D numerical results obtained for the PowerPAD using the mathematical formulations presented in Sec. 2 and the numerical scheme described in Sec. 3.

4.1. Imbibition

In [20], the electrodes and absorbent pad of the PowerPAD device were allowed to become fully saturated before it was used to energize three different external loads: 500 Ω, 1000 Ω, and 2000 Ω. Although the time needed by the system to become fully-saturated was not reported in Ref. [20], the present model is capable of simulating this initial transient mode of operation during activation of the cell. Fig. 5 shows typical results obtained for the 4h-pad system during this initial mode (*i.e.,* before the cell becomes fully-saturated). The cell becomes fully-saturated after roughly t = 12.5 s. Interestingly, when the equilibrium is established, for the electrode we have S = 1 while for the pad the saturation is merely S = 0.93. This observation is a direct consequence of imposing the flux and capillary-pressure boundary conditions at the electrode/pad interface which gives rise to saturation

Downloaded from https://iranpaper.ir
https://www.tarjomano.com ترجمه تخصصی این مقاله مورد تایید ایران پیپر

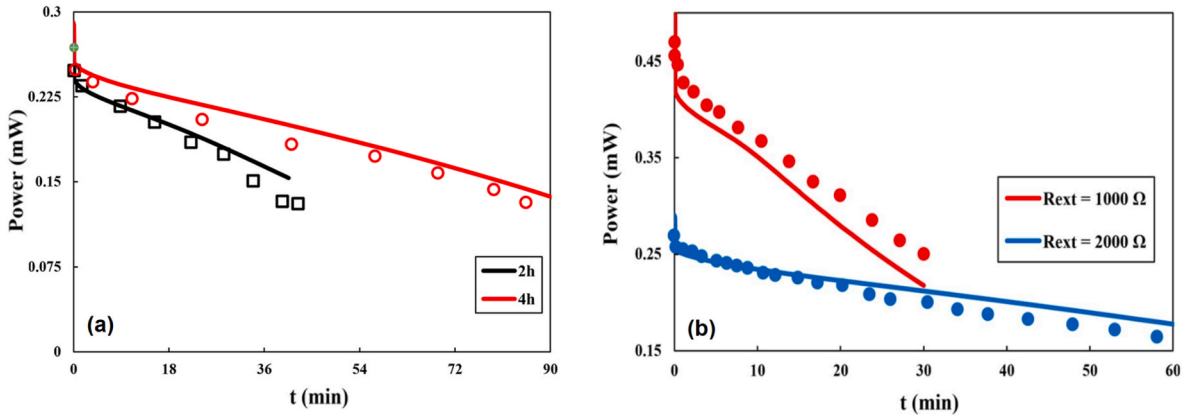

Fig. 4. Recovering the unsteady power performance of the PowerPAD: (a) effect of pad thickness for a 2000 Ω load; and (b) effect of the external load for a 4h-pad system. Model and experimental data [20] are shown by solid lines and symbols, respectively.

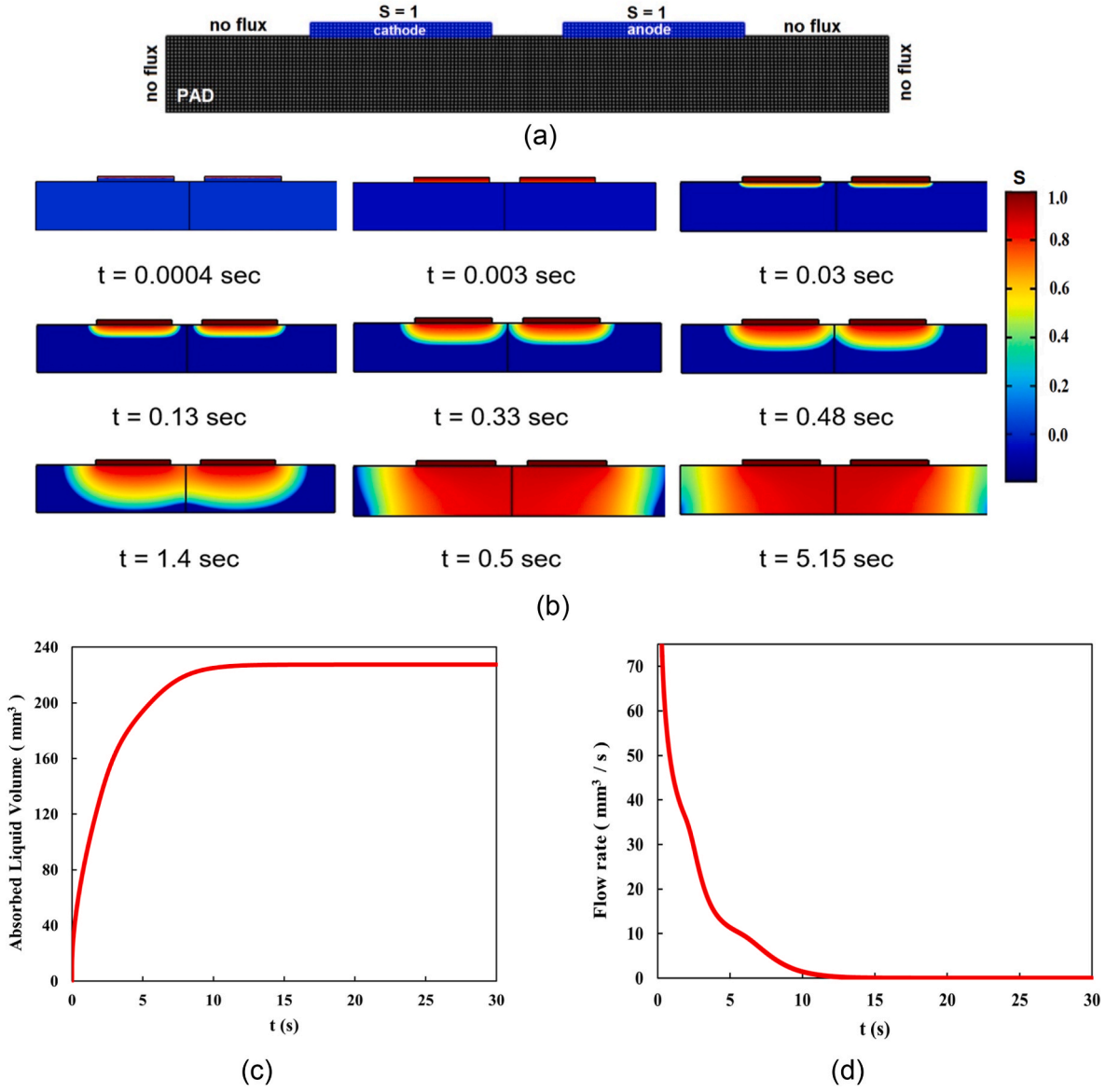

Fig. 5. Imbibition results during the initial transient activation phase of the 2D model for the PowerPAD: (a) computational domain showing the saturation boundary condition at the inlet plane of the electrodes with no-gradient imposed on all other planes; (b) saturation field as a function of time; (c) volume of liquid absorbed by the system over time; and (d) instantaneous flow rate. The results are for the 4h-pad system.

Downloaded from https://iranpaper.ir
https://www.tarjomano.com ترجمه تخصصی این مقاله مورد تایید ایران پیپر

discontinuity at the interface. More specifically, for the interfacial boundary conditions we have [22]:

$$p_{c,e} = P_{c,p} \Rightarrow S_p = \left(\frac{p_{min,e}}{p_{min,p}}\right)^{-\lambda_2} S_e^{\left(\frac{\lambda_p}{\lambda_e}\right)} \tag{67}$$

$$\hat{n} \cdot q_1 = \hat{n} \cdot q_2 \Rightarrow \hat{n} \cdot k_1 \nabla p_{c,1} = \hat{n} \cdot k_2 \nabla p_{c,2} \Rightarrow$$

$$\left(\frac{1}{\lambda_e}\right)(k_{max,e})p_{min,e} \; S_e^{\left(2+\frac{1}{\lambda_e}\right)} \left(\frac{\partial S_e}{\partial z}\right) = \left(\frac{1}{\lambda_p}\right)(k_{max,p})p_{min,p} \; S_p^{\left(2+\frac{1}{\lambda_p}\right)} \left(\frac{\partial S_p}{\partial z}\right) \tag{68}$$

where subscripts e and p refer to the electrode and pad, respectively.

Another look at Fig. 5a reveals that the two electrolytes meet each other at the mid-plane of the pad at t = 0.33 s. Although the cell could conceivably generate power after t = 0.33 s, the capillary flow is likely too rapid and of insufficient duration for the cell to supply any meaningful power during this short period of time. A fully-saturated cell operating based on back-diffusion mechanism is generally more practical because it can generate power for an hour or more, as opposed to seconds for the initial transient activation flow regime. Thus, the results in the next section focus on simulation of the unsteady device operation after activation. The imbibition results also show that the Reynolds number is always in the creeping range during the device activation process corroborating that Darcy's equation is indeed applicable to PowerPAD [37].

4.2. Back diffusion

The experimental data presented in Ref. [20] suggest that there is a cut-off power at a certain time (which depends on the load and pad thickness) at which the cell performance suddenly drops. This behavior of the 3D cell can be captured by the present 2D unsteady model. To study this, we start with showing the time-dependent species concentration fields and power output curves which are used to reveal the core working mechanism of the cell, *i.e.,* the back-diffusion phenomenon. Fig. 6a shows the simulated contour plots for the fuel (H_2BQS) and product (BQS) concentrations at t = 5 and 60 min. These plots show that the fuel conversion at the anode electrode gives rise to an inverted vertical concentration gradient from the bottom of the absorbent pad to the electrode surface. As seen in Fig. 6b, at t = 100 min some fuel has crossed over to the positive side of the cell. Fuel crossover to the positive half-cell and cathode can better be seen in Fig. 6c. This figure clearly shows that, at t = 100 min, the crossed-over fuel has indeed diffused into the cathode through its inner lower corner.

The simulated power output of the cell as a function of time (at fixed load) based on the 2D mathematical/numerical model is presented in Fig. 7, which further shows that the 2D model can correctly predict the time-decaying behavior of the 3D cell [20]. This figure also shows that

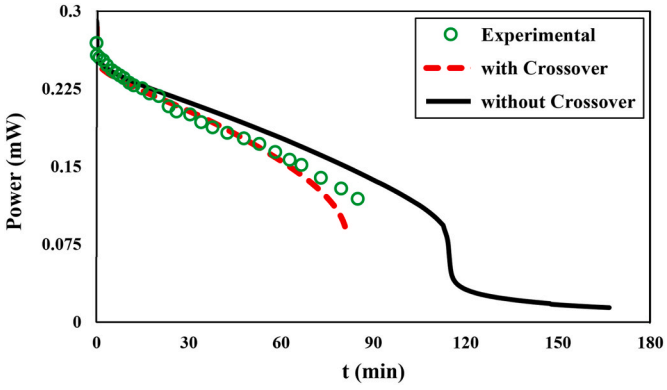

Fig. 7. Comparison of the unsteady cell performance simulated by the 2D model (with and without parasitic side-reactions) and experimental data for the 3D PowerPAD cell. All results shown are for the 4h-2000 Ω system.

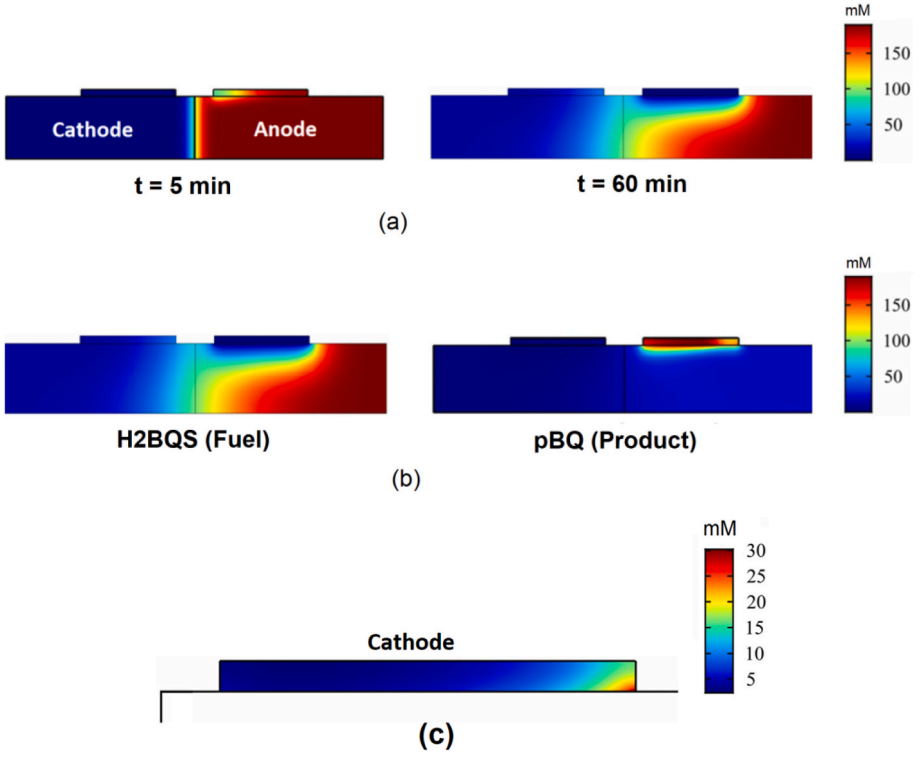

Fig. 6. (a) Simulated concentration of fuel after 5 and 60 min of device operation; (b) simulated concentration of fuel and product at t = 100 min; (c) amount of fuel crossed over to the cathode after t = 100 min. All results shown are for the 4h-2000 Ω system.

iranpaper Downloaded from https://iranpaper.ir
https://www.tarjomano.com ترجمه تخصصی این مقاله مورد تایید ایران پیپر

around t = 110 min there is a sudden drop in the power output which corresponds to a simultaneous sudden drop in both voltage and current (not shown here). To explain these phenomena, it should be noted that as soon as the cell is connected to an external load, the reactants residing inside the electrodes start being consumed (see Fig. 5a). If there were no reactants inside the absorbent pad, the electrodes would be depleted of their active species within a few minutes. In practice, this would have exhibited itself by the power output rapidly dropping to zero. In the present cell design, however, the cell continues to generate power over a much longer time period (~110 min or more) because of the sustained supply of reactants to the electrodes from the underlying absorbent pad. This phenomenon, which is called *back-diffusion* in this work, appears to be the main reason why the cell works for such a long time. The back-diffusion mechanism is facilitated by the inverted vertical concentration gradient, as seen in Fig. 7. According to Fick's equation, this causes the fuel to diffuse back from the pad to the anode. However, as time progresses, the concentration gradient becomes progressively weaker, implying that the power output of the cell should decrease with time, which is indeed observed in Fig. 6.

To explain why the power suddenly drops, it should be noted that for a sufficient amount of fuel to diffuse back to the anode and react electrochemically, the product (BQS) should also diffuse away from the electrode into the pad, *i.e.,* where its concentration is low. In practice, however, this balance can be distorted as time progresses, as product species accumulate within the electrode while fuel is continuously converted leading to a high ratio of product to fuel at the electrode. This negatively affects the electrochemical performance of the cell due to mass-transfer limitations. As mentioned above, the fuel that has crossed over to the positive side may eventually reach the cathode given enough time; see, Fig. 6b and c. The fuel penetrated to the cathode can undergo parasitic side reactions and this may further reduce the power output and shorten the critical time. Fig. 7 shows that this is indeed the case. This figure also shows that with crossover included in the analysis, the numerical results become closer to the experimental data, suggesting that crossover is indeed a limiting factor in the PowerPAD device [20]. Additionally, as time progresses, protons are continuously consumed in the electrolyte, which leads to reduced ionic conductivity and therefore increased ohmic resistance. Thus, the cell performance may also be vulnerable to ohmic loss as a limiting factor. Evidently, in dynamic mode, the electrochemical performance of the PowerPAD is simultaneously controlled by three types of limiting factors: 1) mass-transfer; 2) crossover; and 3) ohmic loss. The question then arises as to which one is the main factor limiting the runtime and/or power output of the cell. The present results suggest that crossover is the dominant factor in this cell, although this could vary depending on cell design and operating conditions.

4.3. Cell design improvements

With the understanding gained through the present modelling work, there are several methods by which the power-output and runtime of the PowerPAD could be enhanced. Perhaps the simplest idea is to replace the electrodes with a new material with enhanced surface area so that the reaction rate can be improved. Goulet et al. [44,45] have shown that the specific surface area of Toray carbon-papers can be enhanced by an order of magnitude through electro-deposition of carbon nanotubes. Here, we consider Sigracet 25 carbon-paper (SGL) as an alternative electrode for which the specific area is equal to 2×10^5 m^2/m^3 (in contrast to 8.3×10^4 m^2/m^3 for the original Toray electrode [15]). In addition to the electrode microstructure, our exploratory investigations have shown that the cell performance can further be enhanced by:

i) Increasing the gap distance from 2 mm to 3 mm and thereby reducing the crossover;
ii) Filling the gap by the pad (the so-called mixed-flow design) and thereby improving the mass-transfer coefficient; and
iii) Increasing the lateral width of the pad and electrodes from 5 mm to 10 mm and thereby reducing the ionic ohmic resistance while simultaneously increasing the mass transfer rate.

These ideas can be combined with each other to render an *optimized cell* design. While maintaining the overall form factor and dimensions of the PowerPAD [20], the following optimized 2D cell design is proposed using the Sigracet electrode: a = 2 x 10^5 m^{-1}, d = 3 mm, W = 10 mm, L = 5 mm, and H = 3.32 mm; see Fig. 1c.

Fig. 8 shows the electrochemical performance of the optimized cell design compared to that of the baseline design for the 2000 Ω load. While in Fig. 8a–c the effect of crossover is excluded from the simulation, in Fig. 8d its effect is considered. These plots show that the optimized cell design has a longer runtime, a higher power output, and a better energy conversion efficiency as compared with the baseline design. In fact, with crossover included in the simulation the critical time of the optimized cell is roughly tripled (80 min vs. 200 min); see Fig. 8d. This is also true for the power output just before the critical time which is roughly equal to 0.08 mW for the baseline design and 0.23 mW for the optimized design; see Fig. 8d. The maximum efficiency is also increased from 44% for the baseline design to 55% for the optimized design (a 25% increase). Evidently, the optimized cell outperforms the baseline design and this is mainly due to its being less sensitive to crossover. The optimized design also has a flatter power output curve which is desirable. Based on these 2D simulation results, it is predicted that the electrochemical performance of the 3D PowerPAD cell can be enhanced through refining certain geometrical parameters: i) by increasing the thickness of its absorbent pad; ii) by increasing the width of its electrode and/or by employing a new one having a higher specific surface area; iii) by increasing the gap distance between the electrodes; and iv) by extending the absorbent pad so that it fills this gap.

5. Conclusions

In the present work, a general mathematical/numerical modelling framework has been developed to describe and simulate the internal working principles and cell performance of paper-based microfluidic flow cells. A two-dimensional version of the model was used to simulate the electrochemical performance of a novel capillary-driven, paper-based 3D cell called PowerPAD for which published experimental data are available. We have shown that, a 2D model can closely represent a 3D device such as the PowerPAD in unsteady mode of operation provided that the Nernst-Planck equation is aptly adjusted. The refined model was validated against experimental data for the PowerPAD in both steady and unsteady modes of operation. The model could properly identify back-diffusion as the main principle underlying the functionality of this flow cell at prolonged times. The validated model also enabled investigation of the effects of different cell design parameters on the runtime and power output of this prospective flow cell. It was shown that the performance of the cell can be improved using a variety of design refinements; chief among them are the electrode geometry/microstructure, the absorbent pad geometry/microstructure, and the flow architecture. An optimized cell design was proposed which roughly tripled the runtime and power output of the PowerPAD. The optimized cell also exhibited a higher energy efficiency up to 55% after more than 4 h of runtime, considerably higher than that of the original design. The obtained numerical results suggest that although mass-transfer and ohmic-loss limitations are important factors for this cell, the implications of reactant crossover are evident at a much shorter time scale than those introduced by the mass-transfer and ohmic-loss limitations. Thus, crossover was identified as the main *limiting factor* for the overall device performance of the PowerPAD. The mathematical model developed in this work together with the fundamental understanding obtained by validating it against experimental data can be used in the design of future capillary-flow-based electrochemical systems, including biodegradable batteries, fuel cells, and electrolyzers.

Downloaded from https://iranpaper.ir
https://www.tarjomano.com ترجمه تخصصی این مقاله مورد تایید ایران پیپر

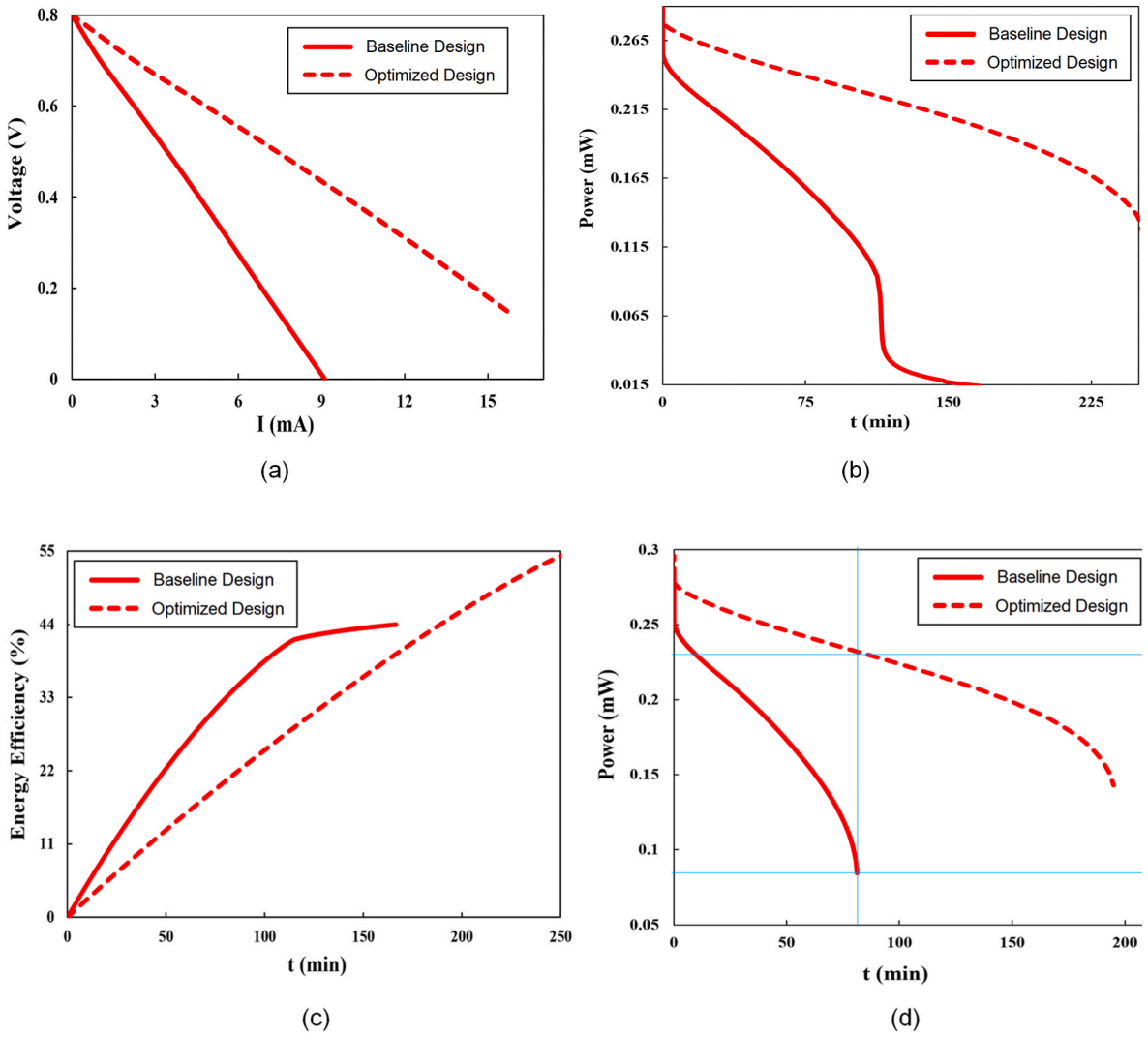

Fig. 8. Simulated cell performance comparison between the baseline design and the proposed optimized design: (a) cell polarization curves; (b) discharge power output curves with parasitic side-reactions excluded; (c) energy conversion efficiency; and (d) power output curves with parasitic side-reactions included. A comparison between plot (b) and plot (d) shows that the optimized design is less vulnerable to crossover side effects than the baseline design.

CRediT authorship contribution statement

P. Sadeghi: Software, Methodology, Data curation, Validation, Investigation, Visualization, Writing – original draft. **E. Kjeang:** Supervision, Project administration, Resources, Conceptualization, Writing – original draft, Writing – review & editing.

Declaration of competing interest

The authors declare that they have no known competing financial interests or personal relationships that could have appeared to influence the work reported in this paper.

Data availability

Data will be made available on request.

Acknowledgements

This research was supported by the Natural Sciences and Engineering Research Council of Canada (NSERC), Canada Foundation for Innovation (CFI), and British Columbia Knowledge Development Fund (BCKDF). This research was undertaken, in part, thanks to the funding received from the Canada Research Chairs program. The authors thank Prof. Mohammad Pourjafar and Dr. Omar Ibrahim for technical advice.

Nomenclature

Roman Definition Unit

A	Area	m^2
a	Specific area	m^{-1}
c	Concentration	mol/m^3
D	Diffusion coefficient	m^2/s
d	Diameter	m

Downloaded from https://iranpaper.ir
https://www.tarjomano.com ترجمه تخصصی این مقاله مورد تایید ایران پیپر

E	Electric potential V
F	Faraday's constant = 96,487C/mol
H	Height of the electrode m
h	Height of the pad m
I	Current A
j	Current density A/m^2
k	Reaction rate constant m/s
k_m	Mass transport coefficient m/s
K	Standard reaction rate constant cm.s^{-1}
L	Length m
N	Molar mass kg/mol
N	Flux density mol/s/m^2
m	Exponent in the Brooks-Corey correlation —
n	Number of electrons —
P	Power mW
p	Pressure Pa
q_{th}	Theoretical capacity mA.hr
Q	Flow rate m^3/s
R	Molar gas constant = 8.314 J/mol/K
R	Ohmic load Ω
S	Moisture content (saturation) —
T	Temperature K
t	Time s
V	Volume m^3
W	Width of electrode m
w	Width of pad m
x	Position vector m
x,y,z	Cartesian coordinates m
Z	Charge number
Greek	Definition Unit
α	Transfer coefficient
β	Volume fraction —
γ	Ionic activity —
μ	Dynamic viscosity mPa.s
ξ	Ionic mobility m^2.mol/J/s
G	Gibbs free energy J/mol
δ	Electrodes gap distance m
ε	Porosity —
θ	Contact angle deg
Θ	Source/sink term mol/m^3/s
φ	Potential V
η	Overpotential V
κ	Permeability m^2
λ	Exponent in the Brooks-Corey Model
ρ	Density kg/m^3
σ	Electric conductivity S/m
σ	Surface tension N/m

Subscripts	*Meaning*
a	Anodic property
c	Cathodic property
eff	Effective value
ext	External ohmic load
th	Theoretical
f	Electrolyte
i	Species
o	Oxidant
r	Reductant
e	Electrode
0	Initial value

Superscripts	*Meaning*
eff	Effective value
eq	Equilibrium value
0	Reference value

Downloaded from https://iranpaper.ir
https://www.tarjomano.com ترجمه تخصصی این مقاله مورد تایید ایران پیپر

s	Surface value
–	Negative electrode
+	Positive electrode

References

[1] I. Buchmann, Batteries in a Portable World: *A Handbook on Rechargeable Batteries for Non-engineers*, third ed., Cadex Electronics Inc., 2011.

[2] J.F. Peters, M. Baumann, B. Zimmermann, J. Braun, M. Weil, The environmental impact of Li-Ion batteries and the role of key parameters–A review, Renew. Sustain. Energy Rev. 67 (2017) 491–495, https://doi.org/10.1016/j.rser.2016.08.039.

[3] K. Saikia, B.K. Kakati, B. Boro, A. Verma, in: Current Advances and Applications of Fuel Cell Technologies. Recent Advancements in Biofuels and Bioenergy Utilization, Springer, Singapore, 2013, pp. 303–337. https://10.1007/978-981-13-1307-3_13.

[4] P. Rewatkara, V.P. Hitaishib, E. Lojoub, S. Goela, Enzymatic fuel cells in a microfluidic environment: status and opportunities. A mini review, Electrochem. Commun. 107 (2019), 106533, https://doi.org/10.1016/j.elecom.2019.106533.

[5] G.L. Soloveichik, Flow batteries: current status and trends, Chem. Rev. 115 (2015) 11533–11558, https://doi.org/10.1021/cr500720t.

[6] R. Ferrigno, A.D. Stroock, T.D. Clark, M. Mayer, G.M. Whitesides, Membraneless vanadium redox fuel cell using laminar flow, J. Am. Chem. Soc. 124 (2002) 12930–12931, https://doi.org/10.1021/ja020812q.

[7] E.R. Choban, L.J. Markoski, A. Wieckowski, P.J.A. Kenis, Microfluidic fuel cell based on laminar flow, J. Power Sources 128 (2004) 54–60, https://doi.org/10.1016/j.jpowsour.2003.11.052.

[8] S. Shrivastava, T.Q. Tung, N.E. Lee, Recent progress, challenges, and prospects of fully integrated mobile and wearable point-of-care testing systems for self-testing, Chem. Soc. Rev. 49 (2020) 1812–1866, https://doi.org/10.1039/C9CS00319C.

[9] A.W. Martinez, S.T. Phillips, G.M. Whitesides, E. Carrilho, Diagnostics for the developing world: microfluidic paper-based analytical devices, Anal. Chem. 82 (2010) 3–10, https://doi.org/10.1021/ac9013989.

[10] A.K. Yetisen, M.S. Akram, C.R. Lowe, Paper-based microfluidic point-of-care diagnostic devices, Lab Chip 13 (2013) 2210–2251, https://doi.org/10.1039/C3LC50169H.

[11] V.T. Nguyen, S. Song, S. Park, C. Joo, Recent advances in high-sensitivity detection methods for paper-based lateral-flow assay, Biosens. Bioelectron. 152 (2020), 112015, https://doi.org/10.1016/j.bios.2020.112015.

[12] J.P. Esquivel, J.R. Buser, C.W. Lim, C. Domínguez, S. Rojas, P. Yager, N. Sabat, Single-use paper-based hydrogen fuel cells for point-of-care diagnostic applications, J. Power Sources 342 (2017) 442–451, https://doi.org/10.1016/j.jpowsour.2016.12.085.

[13] M. Navarro-Segarra, P.P. Alday, D. Garcia, O.A. Ibrahim, E. Kjeang, N. Sabat, J. Pablo Esquivel, An organic redox flow cell-inspired paper-based primary battery, ChemSusChem 14 (2020) 2394–2401, https://doi.org/10.1002/cssc.201903511.

[14] O.A. Ibrahim, M. Navarro-Segarra, P. Sadeghi, N. Sabate, J.P. Esquivel, E. Kjeang, Microfluidics for electrochemical energy conversion, Chem. Rev. 122 (7) (2021) 7236–7266, https://doi.org/10.1021/acs.chemrev.1c00499.

[15] D. Krishnamurthy, E.O. Johansson, J.W. Lee, E. Kjeang, Computational modeling of microfluidic fuel cells with flow-through porous electrodes, J. Power Sources 196 (2011) 10019–10031, https://doi.org/10.1016/j.jpowsour.2011.08.024.

[16] D. Chu, X. Li, S. Zhang, A non-isothermal transient model for a metal-free quinone–bromide flow battery, Electrochim. Acta 190 (2016) 434–445, https://doi.org/10.1016/j.electacta.2015.12.128.

[17] A.A. Shah, M.J. Watt-Smith, F.C. Walsh, A dynamic performance model for redox-flow batteries involving soluble species, Electrochim. Acta 53 (2008) 8087–8100, https://doi.org/10.1016/j.electacta.2008.05.067.

[18] D. Ruiz-Martín, D. Moreno-Boza, R. Marcilla, M. Vera, M. Sánchez-Sanz, Mathematical modelling of a membrane-less redox flow battery based on immiscible electrolytes, Appl. Math. Model. 101 (2022) 96–110, https://doi.org/10.1016/j.apm.2021.08.020.

[19] M. Landeryou, I. Eames, A. Cottenden, Infiltration into inclined fibrous sheets, J. Fluid Mech. 529 (2005) 173–193, https://doi.org/10.1017/S0022112005003356.

[20] J.P. Esquivel, P. Alday, O.A. Ibrahim, B. Fernández, E. Kjeang, N. Sabaté, A metal-free and biotically degradable battery for portable single-use applications, Adv. Energy Mater. 7 (2017), 1700275, https://doi.org/10.1002/aenm.201700275.

[21] L.A. Richards, Capillary conduction of liquids through porous mediums, Phys 1 (1931) 318–333, https://doi.org/10.1063/1.1745010.

[22] R.H. Brooks, A.T. Corey, Hydraulic Properties of Porous Media, in: Hydrology Papers, vol. 3, Colorado State University, Fort Collins, 1964.

[23] S. Suo, M. Liu, Y. Gan, Modelling Imbibition Processes in Heterogeneous Porous Media, *Transp*, vol. 126, Porous Media, 2019, pp. 615–631, https://doi.org/10.1007/s11242-018-1146-7.

[24] H. Huinink, Fluids in Porous Media: Transport and Phase Changes, Morgan & Claypool Publishers, 2016, pp. 1–116.

[25] A. Perez-Cruz, I. Stiharu, A. Dominguez-Gonzalez, Two-dimensional model of imbibition into paper-based networks using Richards' equation, Microfluid. Nanofluidics 21 (2017) 1–12, https://doi.org/10.1007/s10404-017-1937-0.

[26] R. Vodák, T. Fürst, M. Šír, J. Kmec, The difference between semi-continuum model and Richards' equation for unsaturated porous media flow, Sci. Rep. 12 (2022) 7650, https://doi.org/10.1038/s41598-022-11437-9.

[27] G.H. de Rooij, Modeling fingered flow of water in soils owing to wetting front instability: a review, J. Hydrol. 231–232 (2000) 277–294, https://doi.org/10.1016/S0022-1694(00)00201-8.

[28] H. Jensen, V. Devaud, J. Josserand, H.H. Girault, Contact Galvani potential differences at liquid/liquid interfaces: Part I. Experimental studies on single salt distribution at liquid/liquid interfaces using a streaming technique, J. Electroanal. Chem. 537 (2002) 77–84, https://doi.org/10.1016/S0022-0728(02)01250-0.

[29] J. Josserand, G. Lagger, H. Jensen, R. Ferrigno, H.H. Girault, Contact Galvani potential differences at liquid/liquid interfaces: Part II. Contact diffusion potentials in microsystems, J. Electroanal. Chem. 546 (2003) 1–13, https://doi.org/10.1016/S0022-0728(03)00160-8.

[30] Z. Samek, Electrochemistry at the interface between two immiscible electrolyte solutions, Z. Phys. Chemie, Pure Appl. Chem. 76 (12) (2004) 2147–2180, https://doi.org/10.1351/pac200476122147.

[31] R. O'Hayre, S.W. Cha, W. Colella, F.B. Prinz, Fuel Cell Fundamentals, third ed., Wiley, 2016.

[32] C. Brett, A.M. Brett, Electrochemistry: Principles, Methods, and Applications, Oxford University Press, 1993.

[33] P. Stoodley, S. Yang, H. Lappin-Scott, Z. Lewandowski, Relationship between mass transfer coefficient and liquid flow velocity in heterogenous biofilms using microelectrodes and confocal microscopy, Biotechnol. Bioeng. 56 (6) (1997) 681–688, https://doi.org/10.1002/(SICI)1097-0290(19971220)56:6<681::AID-BIT11>3.0.CO;2-B.

[34] Q. Xu, T.S. Zhao, Determination of the mass-transport properties of vanadium ions through the porous electrodes of vanadium redox flow batteries, Phys. Chem. Chem. Phys. 15 (2013) 10841–10848. https://10.1039/C3CP51944A.

[35] J.L. Barton, F.R. Brushett, A one-dimensional stack model for redox flow battery analysis and operation, Batteries 5 (2019) 1–25, https://doi.org/10.3390/batteries5010025.

[36] G. Bruggeman, Calculation of various physics constants in heterogeneous substances, Ann. Phys. 416 (7) (1935) 636–664, https://doi.org/10.1002/andp.19354160705.

[37] P. Sadeghi, *Numerical Modelling of Paper-Based Microfluidic Flow Cells*, Master's Thesis, Simon Fraser University, December, 2021.

[38] M.L. Perry, J.D. Saraidaridis, R.M. Darling, Crossover mitigation strategies for redox-flow batteries, Curr. Opin. Electrochem. 21 (2020) 311–318, https://doi.org/10.1016/j.coelec.2020.03.024.

[39] S.E. Ibáñez, A.E. Quintero, P.A. García-Salaberri, M. Vera, Effects of the diffusive mixing and self-discharge reactions in microfluidic membraneless vanadium redox flow batteries, Int. J. Heat Mass Tran. 170 (2021), 121022, https://doi.org/10.1016/j.ijheatmasstransfer.2021.121022.

[40] I.B. Sprague, D. Byun, P. Dutta, Effects of reactant crossover and electrode dimensions on the performance of a microfluidic based laminar flow fuel cell, Electrochim. Acta 55 (2010) 8579–8589, https://doi.org/10.1016/j.electacta.2010.07.035.

[41] B. Yang, L. Hoober-Burkhardt, F. Wang, G.K. S Prakash, S.R. Narayanan, An inexpensive aqueous flow battery for large-scale electrical energy storage based on water-soluble organic redox couples, J. Electrochem. Soc. 161 (9) (2014) A1371–A1380, https://doi.org/10.1149/2.1001409jes.

[42] T. Haisch, H. Ji, C. Weidlich, Monitoring the state of charge of all-vanadium redox flow batteries to identify crossover of electrolyte, Electrochim. Acta 336 (2020), 135573, https://doi.org/10.1016/j.electacta.2019.135573.

[43] M. Skyllas-Kazacos, M. Kazacos, State of charge monitoring methods for vanadium redox flow battery control, J. Power Sources 196 (20) (2011) 8822–8827, https://doi.org/10.1016/j.jpowsour.2011.06.080.

[44] M.A. Goulet, A. Habisch, E. Kjeang, In situ enhancement of flow-through porous electrodes with carbon nanotubes via flowing deposition, Electrochim. Acta 206 (2016) 36–44, https://doi.org/10.1016/j.electacta.2016.04.147.

[45] M.A. Goulet, O.A. Ibrahim, W.H. J Kim, E. Kjeang, Maximizing the power density of aqueous electrochemical flow cells with in operando deposition, J. Power Sources 339 (2016) 80–85, https://doi.org/10.1016/j.jpowsour.2016.11.053.